Journal of Geophysical Research: Oceans

RESEARCH ARTICLE
10.1029/2018JC014091

Seaglider Surveys at Ocean Station Papa: Oxygen Kinematics and Upper-Ocean Metabolism

Noel A. Pelland[1,2], **Charles C. Eriksen**[1], **Steven R. Emerson**[1], **and Meghan F. Cronin**[3]

[1]School of Oceanography, University of Washington, Seattle, WA, USA, [2]Now at NOAA Alaska Fisheries Science Center, Seattle, WA, USA, [3]NOAA Pacific Marine Environmental Laboratory, Seattle, WA, USA

Key Points:
- Oxygen balances during Seaglider surveys at Ocean Station Papa (50 degrees north, 145 degrees west) were strongly three-dimensional and changed markedly with depth
- Omitting horizontal advection would have led to a 50% overestimate of surface ocean annual net community production
- Autonomous vehicle surveys are a viable method of resolving advection and turbulent mixing terms in the oxygen balance

Supporting Information:
- Supporting Information S1
- Data Set S1

Correspondence to:
N. A. Pelland,
nap2@u.washington.edu

Citation:
Pelland, N. A., Eriksen, C. C., Emerson, S. R., & Cronin, M. F. (2018). Seaglider surveys at Ocean Station Papa: Oxygen kinematics and upper-ocean metabolism. *Journal of Geophysical Research: Oceans*, *123*, 6408–6427. https://doi.org/10.1029/2018JC014091

Received 17 APR 2018
Accepted 10 AUG 2018
Accepted article online 23 AUG 2018
Published online 12 SEP 2018

Abstract Understanding variability in annual net community production (NCP) and factors affecting its estimation are important priorities for the study of ocean biogeochemistry. The time evolution of dissolved oxygen is useful proxy for NCP if the physical tendency can be isolated and removed; a key challenge is the resolution of the terms contributing to this tendency. Here oxygen balances are examined in the upper 200 m at Ocean Station Papa (50°N, 145°W) using data from Seaglider surveys June 2008 to January 2010. Sampling of horizontal gradients of oxygen, temperature, and salinity during these surveys allows the inference of monthly three-dimensional advection and turbulent diffusion of oxygen. The resulting monthly oxygen balances show strong variability with depth, with similarities to the temperature balances shallower than 100 m and salinity balances deeper. The estimated annual NCP of 2.2 ± 1.2 mol C·m^{-2}·year^{-1} in the top 120 m is in agreement with contemporary studies in the subarctic North Pacific Ocean. Horizontal advection in the surface layer is found to be small as previously assumed but important at greater depths: Assuming zero horizontal advection in the top 120 m would have resulted in an overestimate of annual NCP by 50%. Horizontal and vertical advection together dominated the oxygen balance in the permanent pycnocline. Results emphasize the three-dimensional nature of the oxygen balance, even in this relatively quiescent location, and further demonstrate the viability of autonomous spatial surveys for resolving physical oxygen transport terms.

Plain Language Summary In the same manner as plants on land, small organisms in the surface of the ocean produce oxygen and organic carbon through photosynthesis. Some of this carbon sinks to the deep ocean in a process known as the ocean's *biological pump*. Over long periods of time, the biological pump is important for regulating the concentration of carbon dioxide, an important greenhouse gas, in the Earth's atmosphere. One way to measure the biological pump is by monitoring changes in ocean oxygen to determine how much is produced biologically. This study employs this method by deploying small robot submarines, known as ocean *gliders*, to monitor oxygen and ocean flows at a well-studied location in the Gulf of Alaska. The most important finding is that in certain conditions, ocean flows can produce changes in oxygen that are a large fraction of biological production; if they are unaccounted for, they could result in large errors or uncertainties. Encouragingly, results also suggest that gliders—which are a relatively cost effective but still emerging observational technology—are a viable method for estimating such flows. Pairing gliders with other new technologies holds promise for more widespread measurements that could greatly increase our understanding of the biological pump.

1. Introduction

Net community production (NCP) is defined as the net fixation of organic carbon by autotrophic organisms (phytoplankton) in the surface ocean, minus respiration due to autotrophs and heterotrophs (zooplankton and higher-trophic level organisms; Emerson, 2014). At annual time scales or longer, NCP is in approximate equilibrium with *export production* (EP), the flux of organic carbon in particulate or dissolved form from the surface ocean to the interior (Brix et al., 2006). This downward flux of carbon due to the oceanic ecosystem—the ocean's *biological pump*—regulates, in part, the exchange of carbon between the ocean and atmosphere and exerts a fundamental control on the atmospheric concentration of carbon dioxide (Falkowski et al., 2000).

Though a variety of methods have been used to measure or estimate by proxy rates of NCP in the surface ocean, there is a lack of substantial information about its seasonality, relative magnitude in a variety of

oceanic ecosystems, and interannual variability, due to both a scarcity of locations with sufficiently detailed and persistent measurements to allow its estimation and an incomplete understanding or resolution of the physical processes that circulate and redistribute biogeochemical tracers in the surface ocean (Emerson, 2014; Lockwood et al., 2012). This hampers the validation of estimates of NCP from ocean ecosystem models and satellites and inhibits the ability to simulate, diagnose, and assess the overall climate system. Further understanding of variability in NCP and factors affecting its estimation are thus important priorities for the broader understanding of ocean biogeochemistry.

A commonly used tracer to estimate NCP is dissolved oxygen, which through advances in instrumentation can be measured from sensors mounted on moorings or autonomous platforms (Bushinsky & Emerson, 2015; Emerson & Stump, 2010; Hennon et al., 2016; Martz et al., 2008; Nicholson et al., 2008; Plant et al., 2016) and whose production or consumption can be linked to organic carbon using the approximately known stoichiometry of NCP (Emerson & Hedges, 2008). When NCP is positive and net autotrophic conditions persist (i.e., production overcomes respiration), oxygen concentration following a fluid element increases in the absence of mixing. A conservation equation for dissolved oxygen concentration appropriate to the upper ocean reads (Burchard, 2002; Gill, 1982; Kundu & Cohen, 2008; supporting information Text S1)

$$\frac{\mathrm{D}[\mathrm{O}_2]}{\mathrm{D}t} = -\frac{\partial}{\partial z}\overline{w'[\mathrm{O}_2]'} + J^{\mathrm{bio}}, \tag{1}$$

where $[\mathrm{O}_2]$ is the concentration of dissolved oxygen per unit mass of seawater (μmol/kg); $\mathrm{D}/\mathrm{D}t$ ($\equiv \partial/\partial t + u\partial/\partial x + v\partial/\partial y + w\partial/\partial z$) is the derivative following a fluid element; (u, v, w) are, respectively, the zonal, meridional, and vertical components of velocity; $\overline{w'[\mathrm{O}_2]'}$ is the vertical turbulent flux of oxygen per unit mass; and J^{bio} is the rate of change of $[\mathrm{O}_2]$ due to the net biological production or respiration of oxygen.

In principle, (1) can be used to estimate J^{bio} as the difference between the rate of change of $[\mathrm{O}_2]$ following a fluid element (left-hand side) and the convergence of turbulent transport (first term on the right-hand side), if these terms are known. Commonly, this approach is applied in the surface ocean, in an attempt to estimate the net biological production of oxygen in the euphotic zone (e.g., Alkire et al., 2012; Bushinsky & Emerson, 2015; Emerson, 1987; Emerson et al., 1997, 1991, 2008; Emerson & Stump, 2010; Giesbrecht et al., 2012; Hamme & Emerson, 2006; Howard et al., 2010; Izett et al., 2018; Juranek et al., 2012; Nicholson et al., 2008; Palevsky et al., 2016; Plant et al., 2016; Riser & Johnson, 2008; Yang et al., 2017), though it can also be applied to estimate biological oxygen consumption in the deep ocean (e.g., Feely et al., 2004; Hennon et al., 2016; Martz et al., 2008) to obtain a more direct estimate of EP.

Principal difficulties in the application of (1) are the estimation of the advection and turbulent flux of dissolved oxygen. Even at well-sampled time series sites, it is rare to achieve over long durations the simultaneous measurement of gradients and upper-ocean circulation necessary to estimate horizontal advection of oxygen. Persistent sampling of turbulent fluxes is yet more rare, while vertical advection is essentially unmeasurable. Often, the unresolved contribution of these terms must then be either neglected or estimated using remote sensing and climatological data sets. Here we describe results from a field experiment intended to address these uncertainties, through the persistent sampling of three-dimensional spatial gradients of oxygen and other tracers using autonomous vehicle surveys over an 18-month period at Ocean Station Papa (OSP; 50°N, 145°W) in the southern Gulf of Alaska (GOA; Pelland et al., 2016, hereinafter PEC1). Importantly, these measurements allow the use of least squares (*inverse*) methods to obtain time- and depth-varying estimates of horizontal flows along with unmeasured turbulent diffusion and vertical velocity in the upper ocean, which have been shown to successfully describe the bulk evolution of abiotic tracers during the same period (Pelland et al., 2017, hereinafter PEC2). In what follows, these results are applied to the balance of dissolved oxygen, with the goals of examining the balance in various depth ranges and estimating rates of biological production and consumption of oxygen in the upper ocean.

2. Methods

2.1. Seaglider Data

Three individual Seaglider deployments collected measurements of temperature, salinity, pressure, optical backscatter and fluorescence, and $[\mathrm{O}_2]$ from 8 June 2008 to 18 January 2010 while repeating a bowtie survey pattern inscribed within a 50 × 50-km box around the National Oceanic and Atmospheric Administration Ocean Climate Stations mooring at OSP (Hamme et al., 2010; PEC1; Pelland, 2015), in a similar configuration

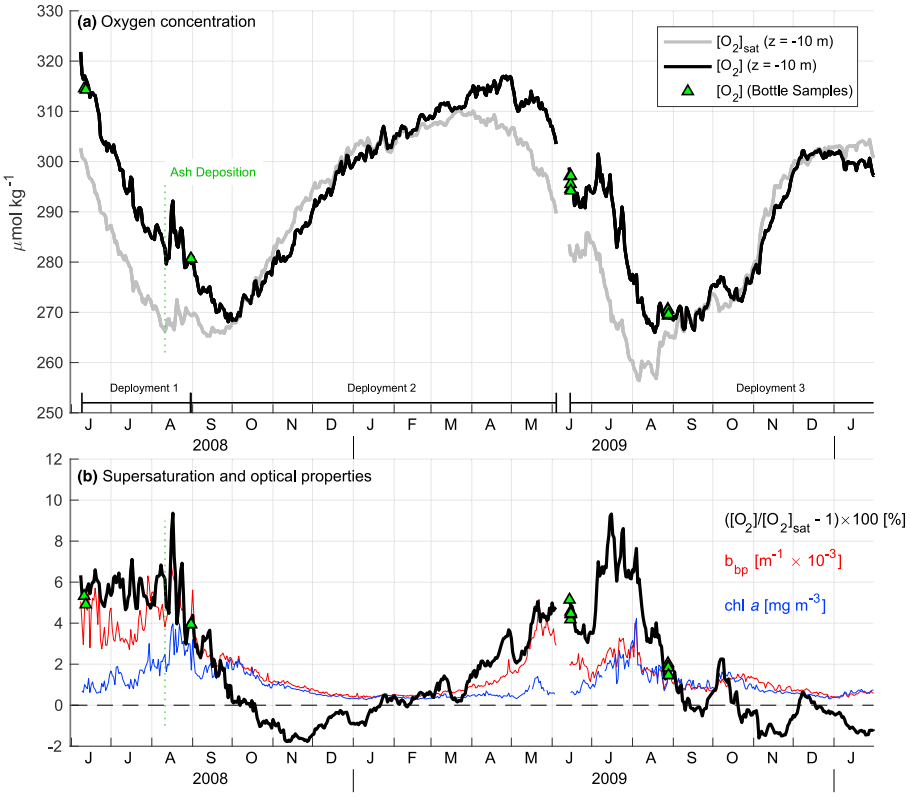

Figure 1. (a) Daily average measurements of dissolved oxygen concentration $[O_2]$ (black curve) and concentration at saturation equilibrium $[O_2]_{sat}$ (Garcia & Gordon, 1992; gray curve) at 10-m depth from Seagliders at Ocean Station Papa (OSP). Labels at bottom indicate the temporal intervals corresponding to each deployment. (b) Daily average supersaturation $([O_2]/[O_2]_{sat} - 1) \times 100$, particulate scattering coefficient b_{bp}, and approximate chl *a* at 10-m depth. Triangles in (a) and (b) indicate surface layer average $[O_2]$ and supersaturation, respectively, estimated from Winkler titrations performed aboard the CCGS *John P. Tully* or R/V *Thomas G. Thompson* during visits to OSP. Green dashed line in each plot indicates approximate date of volcanic ash deposition at OSP (11 August, Hamme et al., 2010).

to previously conducted surveys at the Hawaii Ocean Time Series (HOT) site (Emerson et al., 2008; Nicholson et al., 2008). Seagliders repeated the navigational pattern on average once every 14.5 days, collecting a median 86 vertical profiles along a 1:3 vertical:horizontal glide slope. Seaglider 144 was deployed from 8 June to 30 August 2008 (deployment 1), Seaglider 120 from 30 August 2008 to 14 June 2009 (deployment 2), and Seaglider 144 again from 14 June 2009 to 18 January 2010 (deployment 3; Figure 1a). Seaglider 144 proceeded shoreward along Line P—a set of hydrographic stations between OSP and the Strait of Juan de Fuca—from 18 January to 2 April 2010 (PEC1). At the end of deployment 2, Seaglider 120 ceased profiling on 4 June 2009 due to a low battery state, resulting in a 10-day gap in profiling prior to Seaglider 144's final deployment.

Each vehicle sampled $[O_2]$ using two sensors: a SeaBird Electronics SBE-43 Clark-type electrode sensor and an Aanderaa Data Instruments 3830 oxygen optode sensor. This study uses results from only the optode sensor. The optode models used in this study report a calibrated phase shift quantity (*dphase*) at each sample, which is used with Seaglider temperature estimates to determine oxygen concentration using a manufacturer-supplied polynomial (Aanderaa Data Instruments, 2004). Corrections for salinity and pressure effects were applied following Bittig, Körtzinger, Johnson, et al. (2018) and Uchida et al. (2008), respectively. Optode samples were adjusted for drift in sensor gain and offset at zero concentration (Bittig, Körtzinger, Neill, et al., 2018; Nicholson & Feen, 2017), which were determined by a linear regression fit of optode oxygen versus Winkler titration of bottle samples collected during five ship visits to OSP or along Line P during the Seaglider time series (June and August 2008–2009 and February 2010; Appendix A). At typical surface oxygen values,

the linear regression fits have uncertainties ranging from ±0.27% of saturation (August 2009) to ±0.98% of saturation (August 2008 comparison to SG120 samples), with an average value of ±0.66% (supporting information Figures S4–S9). Within the uncertainty bounds on the regression coefficients, the sensors exhibit a decline in gain and increase in zero offset with time since factory calibration that is consistent with other optode instruments (Appendix A; Bittig, Körtzinger, Neill, et al., 2018). The estimated gain and offset for each instrument were linearly interpolated through time between comparison points. Since Seaglider 120 ceased profiling 10 days before comparison casts were available at the end of its deployment, its final gain and offset were determined by comparison to adjusted Seaglider 144 samples along isopycnals below the surface layer (Appendix A). No correction for optode sensor time lag was applied; this is discussed further in section 4.

In each vertical cast, all scalar variables including adjusted oxygen samples were bin averaged in depth to create a profile on a vertical depth grid with spacing every 2 m from 0- to 150-m depth and every 5 m thereafter to 200 m, resulting in 86 depth bins in the upper 200 m. For every depth bin, horizontal gradients of dissolved oxygen concentration $\nabla[O_2]$ were estimated using least squares multivariable regression fits as a function of time and space to data selected within each of 20 calendar months in which Seaglider surveys took place (PEC1). These monthly intervals—roughly the time required for a vehicle to perform two complete surveys—form the time steps at which all calculations are performed, as will be described below. Ninety-five percent confidence ellipses on the monthly horizontal gradients were computed using a statistical resampling of the regression residuals, as described for temperature and salinity in PEC1. For comparison, climatological oxygen gradients at OSP were also obtained from the World Ocean Atlas 2013 annual climatology (Boyer et al., 2013). Profiles estimated at the center of the survey pattern at the beginning and end of each month (PEC2) were used for evaluating the time rate of change of $[O_2]$, while an average vertical profile within the month was used to compute vertical derivatives.

Optical samples were collected using a Western Environmental Technologies ECO Puck sampling optical backscatter on 470- and 700-nm wavelengths and fluorescence on a single channel with excitation at 470 nm and emission measured at 682 nm. These samples were processed using methods consistent with previous Seaglider applications of this instrument (Pelland et al., 2014; Perry et al., 2008; Sackmann, 2007), which are described in the supporting information (Text S2). Night-only fluorescence measurements were used to avoid the effects of daytime quenching (Sackmann et al., 2008). Optical processing yields estimates of the particulate scattering coefficient (b_{bp}, units of per meter) and relative, though not absolute, chlorophyll a (mg/m^3) (Perry et al., 2008; Sackmann, 2007). For scattering, results from the two wavelengths are qualitatively similar, so only those from the 700-nm wavelength are reported here.

2.2. Estimating the Oxygen Balance

Expanding (1), the rate of change of $[O_2]$ due to production or respiration J^{bio}_{ij} in each depth bin i (= 1, 2, … , 86) and monthly interval j (= 1, 2, … , 20) is estimated as

$$J^{bio}_{ij} = \underbrace{\left.\frac{\partial[O_2]}{\partial t}\right|_{ij}}_{\text{Rate-of-change}} + \underbrace{u_{ij}\left.\frac{\partial[O_2]}{\partial x}\right|_{ij} + v_{ij}\left.\frac{\partial[O_2]}{\partial y}\right|_{ij} + w_{ij}\left.\frac{\partial[O_2]}{\partial z}\right|_{ij} + \frac{\partial}{\partial z}\left(\overline{w'[O_2]'}_{ij}\right)}_{-(\text{Physical Tendency})} + \underbrace{\epsilon_{ij}}_{\text{Error}}. \quad (2)$$

The first term on the right-hand side of (2) is the local rate of change, while the negative of the sum of the second through fifth terms on the right-hand side is the *physical tendency*. The term ϵ_{ij} is the residual error, discussed below. Where estimates of J^{bio} are listed in units of organic carbon C, these have been scaled from oxygen estimates assuming a ratio 1.45:1 O_2:C during photosynthesis and respiration (Hedges et al., 2002).

The physical tendency terms are evaluated using the spatial gradients described above, in addition to horizontal and vertical circulation (u, v, and w) and vertical diffusivity κ results from PEC2, who obtained estimates of these variables by applying a least squares methodology to the time-integrated balances of temperature and salinity in the upper 200 m during Seaglider surveys. In this framework, the vertical turbulent flux and vertical advection are estimated under a set of simplifying assumptions related to the layers of the water column in each month, which are defined to be in order of increasing depth: the well-mixed surface layer, the

stratified transition layer, and the stratified interior. In the stratified layers, where the monthly average density stratification is at least 10% of its maximum value in that month, $\overline{w'[O_2]'} = -\kappa\partial[O_2]/\partial z$. The transition layer is defined as the upper 50 m of the stratified water column. PEC2 estimated a depth-dependent profile of κ within this layer and assumed a constant weak diffusivity in the interior ($\kappa_{INT} = 10^{-5}$ m^2/s). In the surface layer, $\overline{w'[O_2]'}$ is linearly interpolated between its value at the top of the transition layer and a surface value given by the monthly average surface gas exchange, as with turbulent fluxes of temperature and salinity in PEC2. This simplification was made because turbulent fluxes driven by surface heat loss often invalidate the diffusivity parameterization (Large et al., 1994), and monthly profiles of temperature or salinity changes in the surface layer, where turbulent fluxes dominate, were approximately constant, implying a linear turbulent flux (PEC2). This has the consequence that estimated J^{bio} is also vertically constant within the surface layer in each month, which may not be realistic, though J^{bio} integrated across this layer is not impacted because it depends only on the upper and lower turbulent flux boundary conditions. Similarly, w is also linearly interpolated between its uppermost transition layer estimate and the surface, though this does not have a strong impact on the results because vertical gradients of oxygen are weak in the surface layer.

Gas exchange is estimated using a parameterization that explicitly includes the effects of partially and fully collapsing bubbles (Liang et al., 2013) and which has been tested in the North Pacific Ocean for its ability to reproduce the near-surface saturation levels of dissolved nitrogen in one-dimensional models (Bushinsky & Emerson, 2015; Emerson & Bushinsky, 2016; Yang et al., 2017) or to produce NCP estimates similar to those from nitrate balances (Plant et al., 2016). We use a tuned version of this parameterization developed by Yang et al. (2017), who found the best agreement with observational data when fluxes from the bubble components were scaled by a factor β ($\beta < 1$). Two possible values for β were given; we use $\beta = 0.29$, since it was obtained from the one-dimensional kinematic model of Bushinsky and Emerson (2015), which is similar in configuration to that used here. Results with the alternate β value, or with a different gas exchange parameterization also tuned to dissolved nitrogen/oxygen measurements at OSP (Steiner et al., 2007; Woolf & Thorpe, 1991), were not qualitatively different from those presented here (supporting information Text S3). Consistent with the methodology of Yang et al. (2017), exchange was calculated at daily time steps using surface wind speeds derived from the advanced scatterometer instrument (Bentamy & Croize-Fillon, 2012) and sea level pressure values from the National Centers for Environmental Prediction/National Center for Atmospheric Research Reanalysis 1 atmospheric data set (Kalnay et al., 1996), with a bias relative to the OSP mooring removed from the latter (Pelland, 2015, supporting information Text S3).

2.3. Uncertainties

All uncertainty bounds in this study are 95% confidence from an assumed normal distribution. Errors in NCP are assumed to have three components, due to the parameterization of surface gas exchange, the accuracy of glider optode samples, and errors in the physical tendency independent of gas exchange. Uncertainty bounds that reflect the combined effects of all three error types are evaluated using a Monte Carlo procedure with 500 iterations. In each iteration, random errors on oxygen saturation level are drawn at each ship-optode comparison point and interpolated between these points through time. These errors have two components drawn independently: one with 95% bounds that are given by the uncertainty on the regression fit used to determine the optode adjustments (Appendix A and supporting information Figures S4–S9) and one with standard deviation of 0.1% representing uncertainty in the Winkler titration procedure. For deployment 2, the error in the final comparison point (June 2009) is set equal to that of the initial point in deployment 3, before an extra error is added to reflect the uncertainty in the comparison along isopycnals used to determine the gain and offset at the end of deployment 2 (Appendix A and supporting information Figure S11). The local rate of change and surface gas exchange values are then recalculated across the time series, with randomly drawn errors of ±25% and ±10% applied to the bubble and diffusive components of the exchange parameterization, respectively, following Yang et al. (2017).

Values of u, v, w, and κ are resampled in each iteration using the error covariance matrix of the least squares solution estimated in PEC2 (their Appendix B), while errors in monthly horizontal gradients are added based on the confidence bounds described above. The interior diffusivity κ_{INT} is resampled with an uncertainty of ±50% from its assumed value. Advection and diffusion are then recalculated in each iteration using these values and the error-perturbed surface gas exchange. Ninety-five percent confidence bounds on J^{bio}, oxygen concentration, or any components of the physical tendency are then taken as two standard deviations of these quantities estimated across all iterations. For integral results, the integral is computed in each iteration, and the standard deviation of the integral is computed across iterations.

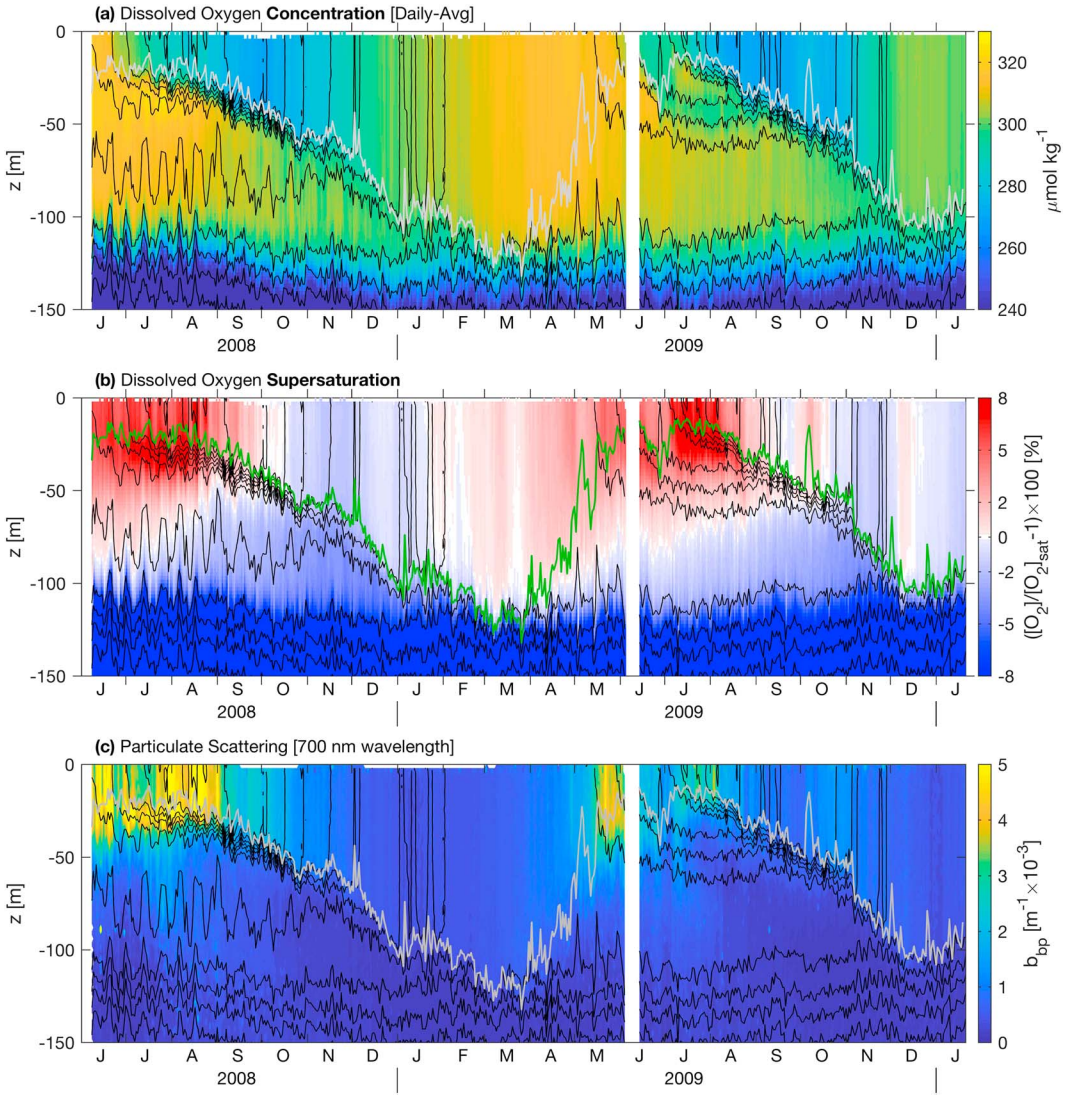

Figure 2. Daily average (a) dissolved oxygen concentration, (b) oxygen supersaturation, and (c) particulate backscattering coefficient b_{bp} versus time and depth. Gray line in (a) and (c) and green line in (b) indicate the daily average of mixed layer depth estimated from individual glider profiles ($\Delta\sigma_\theta = 0.03$ kg/m^3 from 10-m reference value). Black contours in each panel are isopycnals plotted at increments of $\Delta\sigma_\theta = 0.2$. In all panels, where values are outside the plot color range, they are plotted at the maximum/minimum color values.

3. Results

3.1. Upper-Ocean Oxygen and Optical Properties

Dissolved oxygen concentration in the surface layer decreases throughout the summer months at OSP, as the surface ocean warms and solubility decreases and increases thereafter as the mixed layer cools and deepens (Figure 1a). During Seaglider surveys, surface [O_2] was at a minimum in late September/early October 2008 and August/September 2009 and a maximum winter concentration in April 2009. Oxygen concentrations were significantly above saturation equilibrium in the surface layer throughout the summer during Seaglider surveys, coincident with elevated values of surface backscatter and fluorescence, while weak undersaturation or near-neutral saturation states were observed during winter (Figure 1b). Fluorescence values were observed to increase throughout each summer with peak values in late July or August; the maximum supersaturation and backscatter values during the surveys were observed following the deposition of iron-rich volcanic ash in August 2008 (Figure 1b; Hamme et al., 2010), which will be discussed further below.

In the the seasonal thermocline zone (deeper than the surface layer and shallower than the maximum depth of winter mixing, over the depth range 25–120 m in June), weakly supersaturated waters were left behind fol-

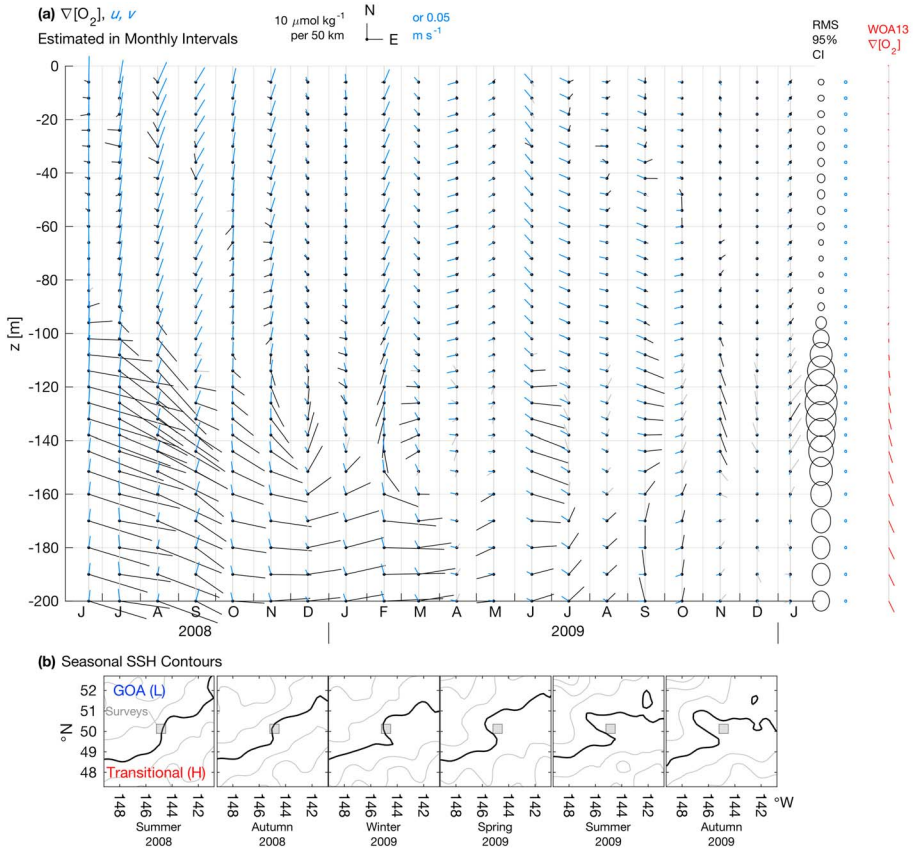

Figure 3. (a) Estimates of monthly horizontal oxygen gradients $\nabla[O_2]$ (black/gray), climatological gradients from WOA13 (red) and circulation *u*, *v* (blue) at selected depths. A vector pointing to the right (up) indicates oxygen increasing, or flow toward, the east (north), with scale at top. Gradients whose confidence ellipses exclude zero are in black, all others in gray. Ellipses at right show RMS 95% confidence bounds on $\nabla[O_2]/u$, *v* by depth. (b) Contours (5-cm interval) of seasonal average SSH in the OSP region during Seaglider surveys, following Pelland et al. (2016). Black contours highlight an evolving meander of the mean flow. SSH is relatively low in the GOA northwest of OSP and high in the subarctic-subtropical transitional domain to the southeast. WOA13 = World Ocean Atlas 2013; RMS = root-mean-square; GOA = Gulf of Alaska; SSH = sea surface height; CI = confidence interval.

lowing mixed layer shoaling in both summers (Figures 2a and 2b). The oxygen concentration steadily declined in this zone thereafter, suggestive of respiration. In the 50- to 100-m depth range, oxygen concentration decreased with time (Figure 2a) and the 0% supersaturation horizon shoaled (Figure 2b) during the months May–October. Elevated particulate scattering and small regions of oxygen supersaturation were apparent in the 10–20 m deeper than the surface layer in summers 2008 and 2009 (Figure 2), suggestive of positive NCP, though supersaturation there can also be generated due to warming. Estimates of productivity in this zone are addressed in section 3.3. Oxygen concentration and saturation state declined steeply with depth in the salinity-stratified upper permanent pycnocline (*halocline*, 120- to 200-m depth; Figures 2a and 2b).

Roughly fortnightly periodicity apparent in $[O_2]$ and density records in summer 2008 in Figure 2 arises from the glider's repeated encounters of spatial variations across its repeat track. Horizontal gradients in dissolved oxygen concentration $\nabla[O_2]$ were strongest in the halocline from June 2008 to March 2009, indicating increasing oxygen toward the east-southeast (black vectors in Figure 3a). During this period, a meander of the North Pacific Current occurred near OSP, as illustrated by seasonal averages of Archiving, Validation, and Interpretation of Satellite Oceanographic data sea surface height (Figure 3b) and horizontal circulation estimated in PEC2 (blue vectors in Figure 3a). This allowed water from the subarctic-subtropical transitional domain normally found to the southeast of OSP to reach the survey region (PEC1). The higher oxygen concentration at a given depth in this water reflects both elevated oxygen concentrations along isopycnals (PEC1), and the greater depth of these isopycnals in the pycnocline (PEC2) in the presence of a positive vertical oxygen gradient (Cummins & Masson, 2012). Confidence ellipses indicate that oxygen gradients were robustly resolved

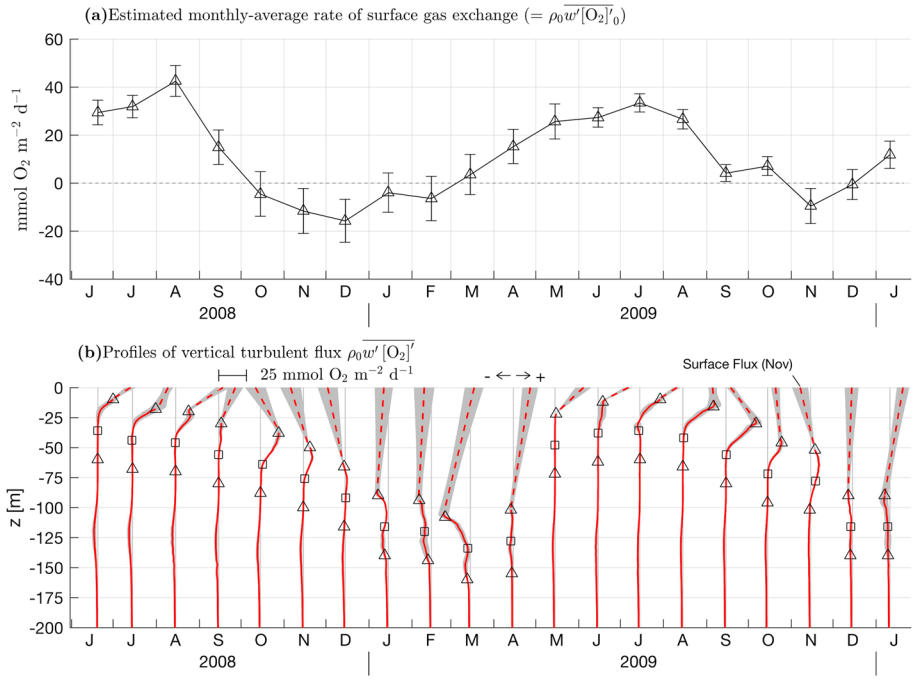

Figure 4. (a) Surface gas exchange and (b) profiles of turbulent dissolved oxygen flux $\rho_0\overline{w'[O_2]'}$ estimated in each monthly time interval. Values in (a) provide the surface boundary condition for the profiles in (b). Whiskers and gray shading indicate 95% confidence bounds. In (b), profiles are offset from the center of each month; positive indicates upward turbulent flux. Triangles plotted on each profile indicate the upper and lower boundaries of the 50-m-thick transition layer; squares indicate its midpoint. Each profile is interpolated between the top of the transition layer and the surface value (dashed line; section 2.2).

in most months and depth intervals with the exception of some portions of the surface layer, the 40- to 80-m depth range in both summers, or the halocline after March 2009 (Figure 3a), where oxygen gradients were weak following the passage of the meander (Figure 3b). Observed horizontal gradients in $[O_2]$ were generally much stronger than the climatological gradients in World Ocean Atlas 2013, which are southeastward in the halocline and near-zero shallower than 80-m depth (profile of red vectors in Figure 3a).

3.2. Kinematics

Monthly average rates of surface gas exchange were estimated to have a maximum outgassing of 43 ± 6 mmol $O_2 \cdot m^{-2} \cdot day^{-1}$ in August 2008 and maximum influx to the surface ocean of -16 ± 9 mmol $O_2 \cdot m^{-2} \cdot day^{-1}$ in December 2008 (Figure 4a). A net outgassing of 6.4 ± 2.3 mol O_2/m^2 was estimated during the time series. If only errors in the optode concentrations are considered in the Monte Carlo simulation, the uncertainty is ± 2.2 mol O_2/m^2. If only parameterization errors are considered, the uncertainty is ± 0.8 mol O_2/m^2.

The values in Figure 4a form the surface boundary conditions for the monthly profiles of vertical turbulent flux (Figure 4b), which are linearly interpolated between the resolved value at the top of the transition layer and the surface. Recall that it is the slope of the turbulent flux profile at a given depth bin that determines the rate of addition or removal of oxygen in the bin due to turbulence (equations (1) and (2). In summer, divergent upward turbulent fluxes remove oxygen from both the surface layer (June–September 2008 and March–August 2009) and the upper transition layer (June–October 2008 and July–October 2009). The upward fluxes in the latter layer are a consequence of the stratification of $[O_2]$ in the summer months at OSP, where the warming surface layer overlies cool, relatively oxygenated water (Figures 2a and 2b). Due to this negative vertical gradient, the turbulent flux of oxygen at the top of the transition layer is upward. In contrast, the convergence of downward fluxes reoxygenates the surface layer in some autumn months (October–December 2008 and September–November 2009, Figure 4b). Everywhere deeper than the upper 25 m of the transition layer, the turbulent fluxes are small in comparison to those in the surface layer, with the exception of the halocline (oxycline) region near $z = -125$ m, where there are strong vertical gradients of oxygen that can result in moderate fluxes of oxygen despite the assumed weak diffusivity there (Figure 4b).

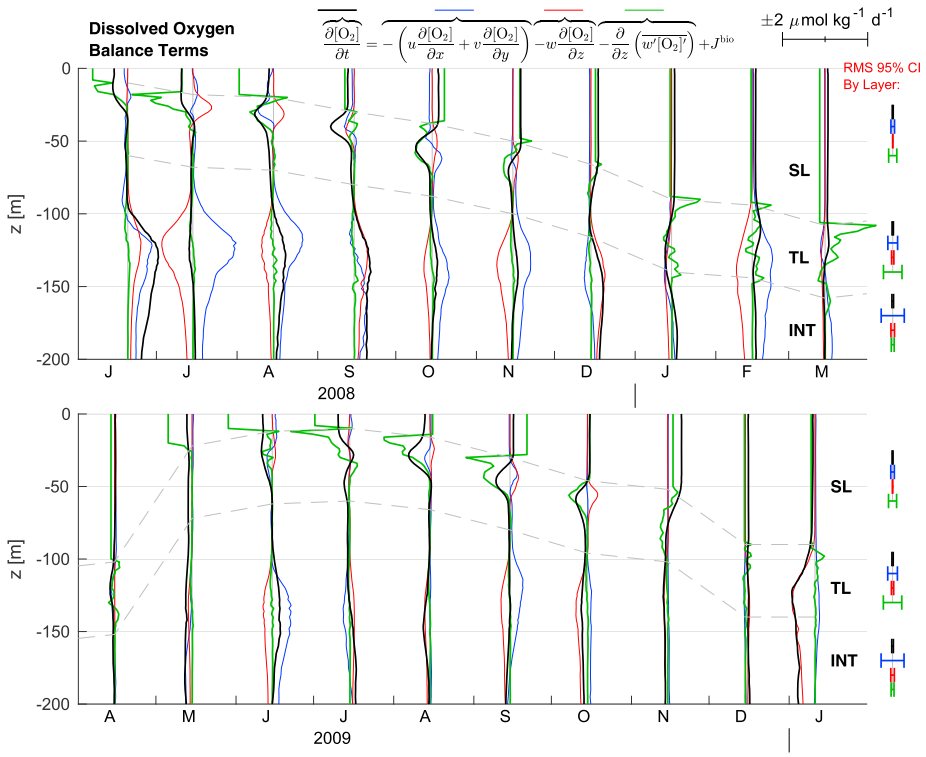

Figure 5. Monthly vertical profiles of resolved terms in the dissolved oygen ($[O_2]$) balance: horizontal advection (blue), vertical advection (red), convergence of turbulent flux (green), and local rate of change (black). Profiles are offset from the center of each monthly interval (scale at upper right). For advection and turbulence terms, positive values indicate a net import of oxygen, that is, advection or diffusion of oxygen that would act to increase the local rate of change, in absence of other effects. Gray dashed lines indicate the time-dependent boundaries between the surface layer (SL), transition layer (TL), and stratified interior (INT). Root-mean-square (RMS) confidence intervals are shown by layer at right.

The divergence or convergence of the turbulent flux profiles, along with horizontal and vertical advection and the local rate of change, are the resolved components of the oxygen balances in each month of this study (Figure 5). Within the surface layer, the divergence of the turbulent transport (gas exchange minus diffusion at the layer base) and local rate of change dominate the resolved terms (Figure 5). Horizontal advection is estimated to play a small role there, removing $< 0.1 \pm 0.1$ mol O_2/m^2 there over the time series, with root-mean-square monthly advection of 0.1 mol $O_2 \cdot m^{-2} \cdot month^{-1}$. During the *growing season* months in which the surface layer is shallow and elevated particulate scattering is evident, horizontal advection removed 0.3 ± 0.1 mol O_2/m^2 in June–October 2008 and imported 0.1 ± 0.1 mol O_2/m^2 in May–October 2009. Horizontal and vertical advection were estimated to be more important in the stratified layers (blue and red curves, Figure 5). All budget terms were small in magnitude in the lower seasonal thermocline (40- to 80-m depth in 2008 and 40- to 100-m depth in 2009), though were much larger in magnitude in the halocline, especially in 2008, partially a consequence of strong spatial gradients of oxygen observed in this zone (Figure 3). In some months, horizontal and vertical advection offset one another (e.g., July 2008 and February 2009), while at other times advection offset the local change (June 2008 and January 2010, Figure 5).

Recall that 120 m forms a natural lower boundary for a vertically integrated dissolved oxygen balance, because of its approximate correspondence with the annual maximum thickness of the surface layer (Freeland, 2013; Martin, 1985; Whitney & Freeland, 1999), and thus, the boundary between the seasonally temperature-stratified upper ocean and salinity-stratified upper permanent pycnocline (PEC1 & PEC2). Figure 6a shows the resolved terms in an oxygen balance integrated vertically across the upper 120 m and temporally from the time series start t_0:

$$\underbrace{\rho_0 \int_{-120\,\mathrm{m}}^{0\,\mathrm{m}} [O_2](z,t)\mathrm{d}z}_{\int_{120}[O_2](t)} = \underbrace{\rho_0 \int_{t_0}^{t}\int_{-120\,\mathrm{m}}^{0\,\mathrm{m}} \left[-u(z,\tau)\frac{\partial[O_2]}{\partial x}(z,\tau) - v(z,\tau)\frac{\partial[O_2]}{\partial y}(z,\tau)\right]\mathrm{d}z\mathrm{d}\tau}_{A_h}$$
$$+ \underbrace{\rho_0 \int_{t_0}^{t}\int_{-120\,\mathrm{m}}^{0\,\mathrm{m}} \left[-w\frac{\partial[O_2]}{\partial z}(z,\tau)\right]\mathrm{d}z\mathrm{d}\tau}_{A_v} + \underbrace{\rho_0 \int_{t_0}^{t} \left[-\kappa(-120\,\mathrm{m},\tau)\frac{\partial[O_2]}{\partial z}(-120\,\mathrm{m},\tau)\right]\mathrm{d}\tau}_{\kappa_{120}}$$
$$+ \underbrace{\rho_0 \int_{t_0}^{t} -\overline{w'[O_2]'_0}(\tau)\mathrm{d}\tau}_{F_{surf}} + \underbrace{\rho_0 \int_{t_0}^{t}\int_{-120\,\mathrm{m}}^{0\,\mathrm{m}} J^{\mathrm{bio}}(z,\tau)\mathrm{d}z\mathrm{d}\tau}_{\int J}$$
$$+ \underbrace{\rho_0 \int_{-120\,\mathrm{m}}^{0\,\mathrm{m}} [O_2](z,t_0)\mathrm{d}z}_{\int_{120}[O_2](t_0)}, \tag{3}$$

where A_h represents horizontal advection, A_v vertical advection, κ_{120} the flux of oxygen into the top 120 m due to turbulent diffusion at the lower boundary, F_{surf} the net loss of oxygen due to gas flux from the ocean surface to the atmosphere $\rho_0\overline{w'[O_2]'_0}$, and $\int J$ the integrated net community productivity/respiration (omitted in Figure 6a). The largest resolved term is the surface gas exchange (Figure 6a). In the top 120-m budget, flow from the south and east (PEC1 & PEC2; Figure 3) was estimated to import 2.8 ± 0.6 mol/m^2 of oxygen, though most of this (1.9 mol/m^2) occurs during June–November 2008 (Figure 6a). Of the 2.8-mol/m^2 total, 2.4 mol O_2/m^2 was imported between 80- and 120-m depth in the months June–November 2008, when horizontal gradients in this zone were strong (Figure 3a), while 0.5 mol O_2/m^2 was removed in these months between the surface and 80-m depth.

In PEC2, a net upwelling of water was estimated (average: 42.5 m/year). In the upper 120 m, the resulting vertical advection is estimated to remove 0.7 ± 0.1 mol/m^2 of oxygen, while turbulent transport at 120 m removes 1.5 ± 0.4 mol O_2/m^2 (Figure 6a). Half of this downward diffusion is estimated during months when the surface layer is deep and boundary layer turbulence penetrates to the halocline: 0.6 mol O_2/m^2 in January–April 2009 and 0.1 mol O_2/m in December 2009 to January 2010, with a mean rate of downward diffusion during these months of 4.2 mmol $O_2\cdot m^{-2}\cdot day^{-1}$. During the remaining months, the assumed $\kappa_{\mathrm{INT}} = 10^{-5}$ m^2/s gives a mean rate of downward O_2 diffusion of 1.8 mmol $O_2\cdot m^{-2}\cdot day^{-1}$.

In a vertically integrated oxygen balance in the halocline (120- to 200-m depth), horizontal and vertical advection are estimated to play dominant roles (Figure 7). Upwelling is more effective at removing oxygen from the halocline than the upper 120 m because of the strong vertical gradient across this zone: Vertical advection of oxygen-depleted water is estimated to remove 7.7 ± 0.4 mol O_2/m^2, while horizontal advection imports 12.0 ± 1.0 mol O_2/m^2 (Figure 7). Turbulent diffusion at the upper and lower boundaries is much weaker than these terms though not negligible in comparison to expected rates of biological consumption of oxygen of ~1 mol $O_2\cdot m^{-2}\cdot year^{-1}$ (Feely et al., 2004; Hennon et al., 2016). Turbulent flux across the lower boundary (κ_{200}) removes 0.5 ± 0.3 mol O_2/m^2, while the 1.5 mol O_2/m^2 removed from the upper 120 m by diffusion (κ_{120}) is a source of oxygen to the halocline.

3.3. Net Community Productivity or Respiration

In the upper 120 m, since the observed oxygen content exceeds the integrated physical tendency beyond the uncertainty bounds, a net biological production of 4.3 ± 2.6 mol O_2/m^2 (3.0 ± 1.8 mol C/m^2) is estimated 8 June 2008 to 21 January 2010 (Figure 6). This is composed of 6.2 ± 2.4 mol O_2/m^2 in the surface layer and 0.8 ± 0.3 mol O_2/m^2 deeper than the surface layer but shallower than 40 m (the *deep euphotic zone*), which is offset by 2.7 ± 0.8 mol O_2/m^2 of respiration deeper than the surface layer or 40 m and shallower than 120 m (the *subeuphotic zone*; Figure 6b).

The top 120 m is an appropriate depth range for calculating upper-ocean annual NCP (ANCP) because of its correspondence to the annual maximum thickness of surface mixing and therefore the approximate depth

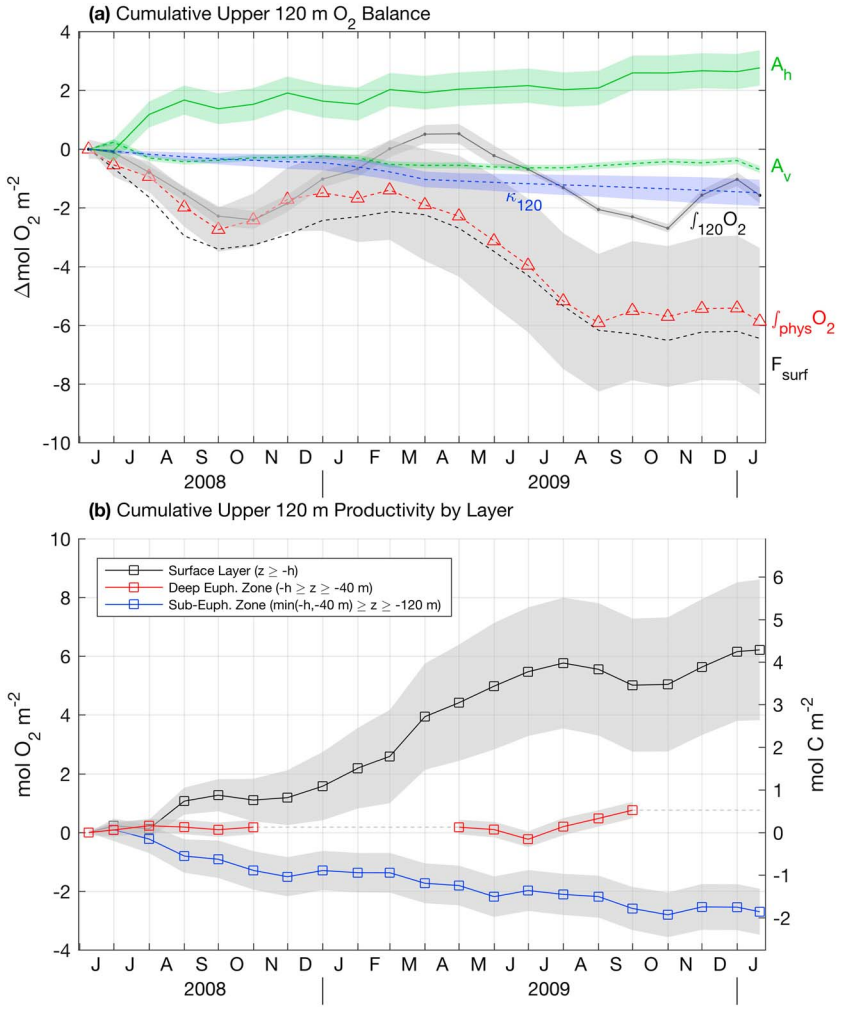

Figure 6. (a) Time-integrated resolved terms in the dissolved oxygen balance in the upper 120 m: oxygen content (black, $\int_{120}O_2$), integrated physical tendency (red dashed, $\int_{phys}O_2$), and its components horizontal advection (green, A_h), vertical advection (green dashed, A_v), diffusion at 120 m (blue dashed, κ_{120}), and surface gas exchange (black dashed, F_{surf}). Shaded regions indicate 95% confidence bounds on each term except F_{surf}. (b) Estimated time-integrated productivity by layer in the upper 120 m (surface, deep euphotic zone, and subeuphotic zone). The deep euphotic zone is defined as deeper than the surface layer but shallower than 40-m depth; correspondingly, the curve for this layer is discontinuous during months when the surface layer is deeper than 40 m.

beyond which organic carbon must be exported in order to be isolated from the surface ocean on an annual basis (Emerson, 2014; Körtzinger et al., 2008; Oschlies & Kähler, 2004; Quay et al., 2012). Dividing the top 120-m integrated NCP by the duration of the surveys likely biases the estimate, because the annual cycle is not evenly sampled in this study. One way to address this is to form a composite annual estimate, in which an average upper 120-m productivity rate is estimated first for each calendar month and then ANCP estimated over this composite year. This method yields an ANCP of 3.1 ± 1.7 mol $O_2 \cdot m^{-2} \cdot year^{-1}$ (2.2 ± 1.2 mol $C \cdot m^{-2} \cdot year^{-1}$). Increasing the depth of integration to 130 m decreases the estimated ANCP by 0.1 mol $O_2 \cdot m^{-2} \cdot year^{-1}$, while decreasing the depth of integration to 110 m increases ANCP by 0.3 mol $O_2 \cdot m^{-2} \cdot year^{-1}$. In the composite estimate, 4.6 ± 1.6 mol $O_2 \cdot m^{-2} \cdot year^{-1}$ is produced in the surface layer, while 1.4 ± 0.5 mol $O_2 \cdot m^{-2} \cdot year^{-1}$ is respired deeper than this layer and shallower than 120 m.

The largest rates of surface productivity per unit area are estimated in March 2009 (44 ± 10 mmol $O_2 \cdot m^{-2} \cdot day^{-1}$ and August 2008 (30 ± 7 mmol $O_2 \cdot m^{-2} \cdot day^{-1}$). Net heterotrophy is indicated in the surface layer in some months (July and October 2008 and August–September 2009; Figure 6b), the strongest rate being −18 ± 6 mmol $O_2 \cdot m^{-2} \cdot day^{-1}$ in September 2009. In the deep euphotic zone, productivity is estimated to be intermittent but positive overall. The greatest rate of productivity (respiration)

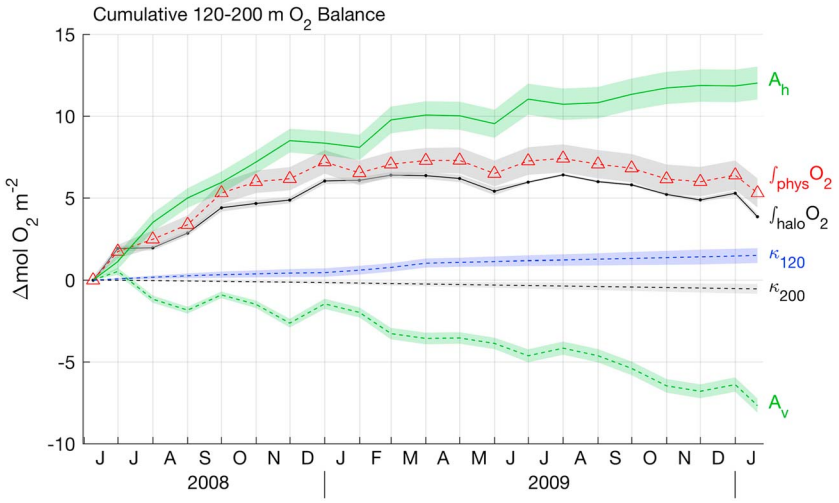

Figure 7. Time-integrated resolved terms in the 120- to 200-m oxygen balance, shown as for 0–120 m in Figure 6a, though note the change of scale in the *y* axis. Here the upper boundary condition for turbulent flux is given by diffusion at 120 m (κ_{120}, the negative of the term shown in Figure 6a), and the lower boundary condition by diffusion at 200 m (κ_{200}).

there was estimated to be 14 ± 4 mmol $O_2 \cdot m^{-2} \cdot day^{-1}$ in July 2009 (−11 ± 4 mmol $O_2 \cdot m^{-2} \cdot day^{-1}$ in June 2009). Respiration was more consistently estimated in the subeuphotic zone, with the strongest rate of −19 ± 9 mmol $O_2 \cdot m^{-2} \cdot day^{-1}$ in August 2008 (Figure 6b). In the halocline, the estimated net addition of oxygen by physical terms exceeds the observed increase in oxygen content after autumn 2008 (Figure 7), giving an estimated NCP there of −1.4 ± 0.9 mol O_2/m^2. Using the annual compositing method gives an annual NCP in the halocline of −1.1 ± 0.6 mol $O_2 \cdot m^{-2} \cdot year^{-1}$.

A vertically smoothed mean profile of NCP $\overline{J^{bio}}(z)$, constructed using the annual compositing described above, is shown in Figure 8. Profiles of J^{bio} in each month were first vertically averaged over the top 25 m of the transition layer before compositing; the resulting profile was then vertically averaged over adjacent sets of five depth bins. These steps are intended to reduce the effects of errors in physical transports and unresolved terms, which as shown in PEC2 can be large at individual depth levels but are much reduced by vertical averaging.

The overall composite profile consists of high near-surface productivity shallower than a layer of moderate net respiration, which due to measurement uncertainty becomes indistinguishable from zero near 140-m depth (Figure 8). This profile shows positive NCP above 90-m depth, indicating that at depths of 40 to 90 m, autumn and winter productivity in the surface layer overcomes summer respiration. A second profile is also shown, which at each depth is an average of J^{bio} only when that depth is within the stratified water column and deeper than the surface layer. This profile is independent of surface gas exchange and illustrates NCP rates in the seasonal thermocline during the growing season. This profile consists of approximately vertically constant rate of oxygen consumption throughout the 40- to 120-m depth range (Figure 8), consistent with steadily declining oxygen concentration observed in this zone during late spring, summer, and early fall (section 3.1). Productivity in the deep euphotic zone is evident in this profile, which supports the choice of a compensation depth, that is, the depth at which gross primary production and community respiration are equal resulting in zero NCP, of 40 m during the growing season.

4. Discussion

In this study, the composition of terms in the oxygen balance, and the overall size of individual terms, was markedly different depending on the vertical zone (Figures 5–7). The balance between local change and convergence of turbulent flux in the surface layer, weak horizontal advection there, and increasing importance of advection with depth in the transition layer are similar to the balance of potential temperature as described in PEC2. By contrast, in the halocline, the offsetting horizontal and vertical advection or advection offsetting local change are similar to, though of opposite sign, the corresponding terms in the salinity balance (PEC2). The strong fluxes and large net changes in oxygen content observed in the halocline are consistent with the

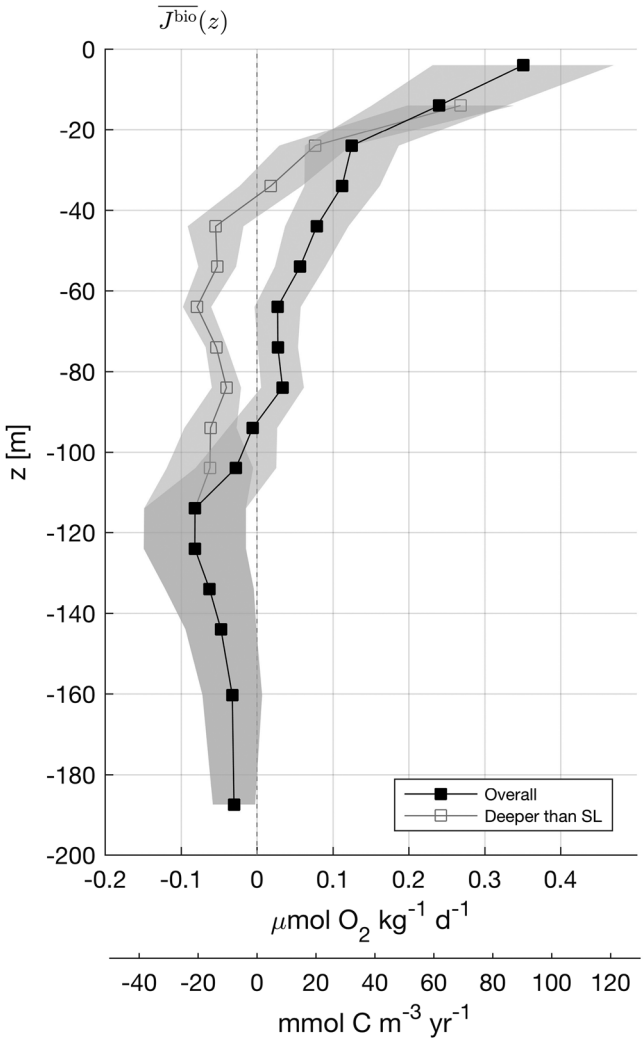

Figure 8. Mean vertical profiles of net community production or respiration $\overline{J^{bio}}$, estimated in composite fashion as described in section 3.3. Estimates are shown for the overall rate profile (black squares) and for a profile that averages J^{bio} at each depth only during periods when that depth is located deeper than the surface layer (SL, gray squares; section 3.3). Shaded gray regions indicate 95% confidence bounds.

results of Tabata (1965), who found that nonseasonal variations dominated the dissolved oxygen content deeper than 125 m in his analysis of early Weathership data from 1956 to 1962. The downward turbulent flux of oxygen across the upper boundary of the halocline, and its variability by season, is in good agreement with the results of Bushinsky and Emerson (2015).

Uncertainty in the upper 120-m productivity in this study was dominated by the surface gas exchange and, in particular, the component due to optode accuracy (section 3.2). Optodes remained submerged while Seagliders were at the surface in this study, but changing the sensor location to facilitate in situ air calibration (Bittig & Körtzinger, 2017; Bittig, Körtzinger, Neill, et al., 2018; Bushinsky & Emerson, 2015)—a method recently adapted for a different glider model by Nicholson and Feen (2017)—could further reduce the uncertainty of similar future studies. Within the uncertainty, the rates of productivity estimated during the 1.6-year Seaglider surveys are in broad agreement with other contemporary investigations in the GOA using oxygen, oxygen/argon ratios, nitrate, or carbonate system parameters (Bushinsky & Emerson, 2015; Fassbender et al., 2016; Palevsky et al., 2016; Plant et al., 2016; Yang et al., 2017), which support an ANCP of 1.5–2.4 mol $C \cdot m^{-2} \cdot year^{-1}$. The observation of net heterotrophy within the surface layer in some months is consistent with other recent studies (Bushinsky & Emerson, 2015; Fassbender et al., 2016; Plant et al., 2016), though here this heterotrophy is not as intense nor as widespread in time. The net respiration of 1.4 ± 0.5 mol $O_2 \cdot m^{-2} \cdot year^{-1}$ deeper than the

surface layer and shallower than the maximum mixing depth is greater than the 0.4 mol $O_2 \cdot m^{-2} \cdot year^{-1}$ estimated south of OSP by Palevsky et al. (2016). Multiple years of three-dimensional sampling would be needed to determine if the above differences are systematic offsets or are instead due only to interannual variability within the limited time extent resolved here.

The result that horizontal advection of oxygen is weak in the surface layer supports the assumptions or inferences of previous investigators at OSP (Emerson, 1987; Emerson & Stump, 2010; Giesbrecht et al., 2012; Izett et al., 2018). However, integrated over the top 120 m, horizontal advection imported an amount of oxygen of the same order as NCP in this study. If horizontal advection had been neglected, the composite ANCP would have increased by 50% to 4.8 mol $O_2 \cdot m^{-2} \cdot year^{-1}$. This suggests that the neglect of horizontal advection deeper than the surface layer may not be justified in the oxygen balance in the subarctic North Pacific Ocean, especially during periods of anomalous flows such as observed during Seaglider surveys (PEC1 & PEC2; Figure 3).

August 2008 featured high particulate scattering and elevated productivity in the surface layer (Figures 1 and 2 and section 3.3) due to the release of iron limitation following an atmospheric deposition of volcanic dust (Giesbrecht et al., 2012; Hamme et al., 2010). Giesbrecht et al. (2012) calculated an NCP rate of 45.9 mmol $C \cdot m^{-2} \cdot day^{-1}$ from an O_2/Ar mass balance in this month; this compares to an estimated rate of 21 ± 5 mmol $C \cdot m^{-2} \cdot day^{-1}$ here. Giesbrecht et al. (2012) neglected diffusion at the base of the surface layer in their mass balance, on the basis of an assumed 10^{-5} m^{-2} s^{-1} upper limit on the diffusivity. This value is weaker than estimated by Cronin et al. (2015) or PEC2, the latter of which showed profiles of κ in all months increasing steeply with height in the upper transition layer to $\mathcal{O}(10^{-4})$ m^2/s or greater. These results are consistent with effective mixing coefficients estimated indirectly at OSP in spring using measurements of N_2O by Izett et al. (2018). A greater diffusivity at the surface layer base would result in a greater flux of oxygen into this layer and lower estimate of productivity (Giesbrecht et al., 2012). On the other hand, in this study, estimates of surface gas exchange in this month were somewhat sensitive to the choice of parameterization (supporting information Text S3 and Figure S3). Using the parameterization tuned at OSP by Steiner et al. (2007) would increase the estimated surface layer productivity in this month by 11 mmol $C \cdot m^{-2} \cdot day^{-1}$.

Evidence of deep euphotic zone productivity at OSP (Figure 8) is consistent with the results of Thomas et al. (1990) who found that it was necessary to explain the observed supersaturation below the surface layer. This production was estimated to be a small fraction of the total euphotic zone productivity, in contrast to results from similar surveys at HOT (Nicholson et al., 2008). The compensation depth of 40 m during summer appears shallower than that at HOT, where productivity was evident as deep as ~100 m (Nicholson et al., 2008). Deeper than the euphotic zone, resolved rates of respiration are comparable to other recent estimates; Feely et al. (2004) report rates of organic carbon remineralization peaking at −6–7 μmol $C \cdot kg^{-1} \cdot year^{-1}$ (−0.024–0.028 μmol $O_2 \cdot kg^{-1} \cdot day^{-1}$) shallower than 200-m depth in Pacific Subarctic Upper Water, which is found in a broad region of the North Pacific Ocean north of ~40°N. These rates are similar to those observed in the halocline in this study (Figure 8). The vertical respiration rate profile of Hennon et al. (2016) in the GOA (their Figure 4), which is comparable to the $\overline{J^{bio}}$ profile outside the SL computed here, is in good agreement shallower than 200-m depth where the vertical domains of the two studies overlap. Although respiration could be resolved when averaged across the halocline in this study, an insufficient fraction of the vertical profile of deep respiration was measured to form a direct estimate of EP. Due to the smaller size of the biological contribution to oxygen tendency in the deep ocean, the use of many independent platforms (e.g., Hennon et al., 2016; Martz et al., 2008) is an advantage when computing EP since mesoscale noise, such as that which contributed to the uncertainty here, is averaged over a basin scale.

In addition to drift following the factory calibration, optode sensors mounted on autonomous floats and gliders have a response time on the order of 10–100 s (Bittig et al., 2014; Bittig & Körtzinger, 2017). This lag results in average differences of 20 μmol/kg in oxygen concentration in the halocline between adjacent ascent and descent Seaglider profiles in this study, which have negative and positive biases, respectively, due to the steep vertical oxygen gradient there. Applying the lag correction method of Nicholson (2009, his Appendix A) to individual profiles reduced the average difference between adjacent profiles in the halocline, but increased the average difference at the base of the surface layer in summer, where oxygen gradients are also large (data not shown). Rather than apply a correction to individual profiles that would reduce error in one layer at the expense of another, we elected to proceed with monthly averaging under the assumption that biases between ascent and descent profiles would largely cancel. The data support this assumption: Monthly aver-

ages of profiles to which the Nicholson (2009) correction had been applied had vertical gradients in the halocline that differed by 1–3% from those without lag correction. Average vertical gradients at the surface layer base in summer differed by 16%, but it is not clear that this is an improvement, since the lag correction reduced agreement between adjacent profiles there, as noted above. These differences would result in a redistribution of estimated NCP within the upper 120 but no difference in vertically integrated productivity in this region, which depends on the lower boundary condition of turbulent flux (equation (3)). Horizontal gradients of oxygen estimated from lag-corrected profiles were negligibly different from those without lag correction. Bittig and Körtzinger (2017) present a more detailed and mechanistic algorithm for correcting lag, but this algorithm was not considered because it relies on empirical estimates of boundary layer thickness versus profiling speed that have not been evaluated for the Seaglider configuration used in this study.

The balance (2) used to estimate J^{bio} assumes that all terms are constant within each monthly interval, thereby excluding oxygen transport processes that may act over shorter time scales (e.g., Omand et al., 2015; Thomsen et al., 2016). This simplification is made out of necessity, since this is the time required for Seagliders to reliably obtain independent realizations of horizontal gradients across the survey pattern (PEC1 & PEC2). Horizontal turbulent terms are also neglected, since parameterizing these would involve computing horizontal curvature of the dissolved oxygen field, which is not resolved well by Seaglider surveys (Pelland, 2015). We note that other studies that have successfully modeled the annual cycle of physical variables (e.g., Large et al., 1994; Martin, 1985) or dissolved oxygen (Steiner et al., 2007; Thomas et al., 1990) at OSP have also made the latter assumption. Furthermore, the results of PEC2 support these assumptions a posteriori for temperature and salinity: The monthly estimates of circulation and diffusivity were shown to reproduce the observed time record of temperature (salinity) at a given depth level with an average error of 19.4% (21.7%) of the variance and were able to reproduce the bulk vertical stratification of both variables in all months but one, capturing seasonal variability in the top 120 m and lower-frequency variability in the halocline. The ability of the circulation and diffusivity values to successfully describe the evolution of two independent, biologically inert tracers in the same time and space domain corroborates the estimates of oxygen advection and diffusion terms in this study.

5. Conclusions

Results of this study demonstrate that the oxygen balance may have important contributions from horizontal advection in the upper ocean even in a relatively quiescent and weakly advective location such as the GOA. During Seaglider surveys at OSP, the neglect of horizontal advection would have resulted in a 50% overestimate of ANCP integrated across the upper 120 m. Horizontal and vertical advection dominated the oxygen balance at greater depths. Autonomous in situ measurement of spatial structure at time series sites is a viable method for the estimation of horizontal advection and inference of vertical advection/diffusion that if otherwise unresolved would add significant uncertainty to biogeochemical rate estimates composed from time series of vertical profiles alone. Here such measurements allowed diagnosis of the oxygen balance across a 50-km square box at monthly intervals; physical processes at finer spatial and temporal scales and their importance to oxygen transport warrant continued investigation at this and other locations. Combining the type of surveys described here with other recent advances in autonomous methods for sampling biogeochemical tracers, such as air calibration of oxygen sensors, measurement of carbonate system parameters, and nitrate sensors mounted on autonomous floats, offers the potential for persistent and increasingly constrained measurement of upper-ocean biological processes relevant to the climate system. Ocean time series sites with a strong base of infrastructure and historical study such as OSP are a logical starting point for such combined approaches.

Appendix A: Oxygen Optode Adjustment

Two individual oxygen optodes were used within the three Seaglider missions in this study. Instrument 1 (S/N 15) was deployed on Seaglider 144 in deployments 1 and 3, while instrument 2 (S/N 26) was deployed on Seaglider 120 during deployment 2 (section 2 and Figure 1). Factory calibrations were performed on 17 January 2008 for instrument 1 and 24 April 2008 for instrument 2. Independent oxygen measurements collected close enough to Seaglider profiles for robust comparison were available from five research vessel visits to OSP or along Line P (Table A1). These measurements were obtained from Winkler titration of bottle samples collected from the CCGS *John P. Tully* or R/V *Thomas G. Thompson*, performed by members of the R. Hamme

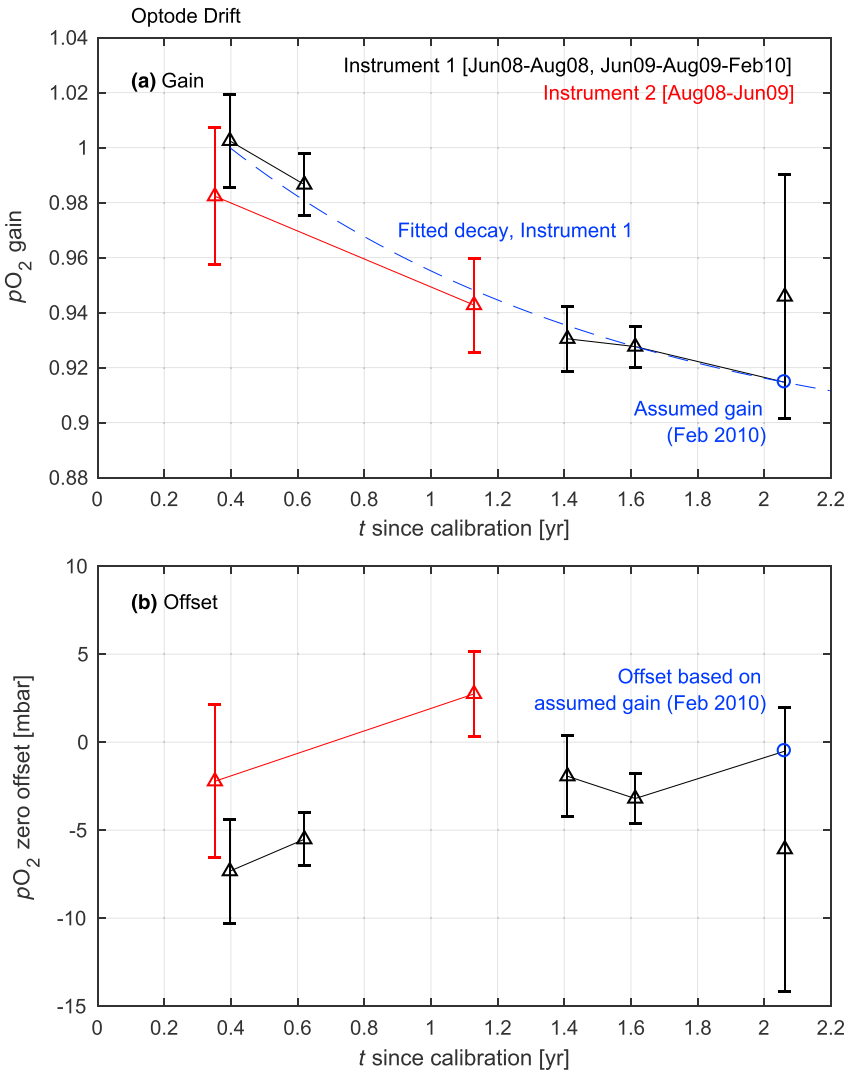

Figure A1. Estimated optode (a) gain and (b) zero offset versus time since calibration for instruments 1 (black) and 2 (red). Gain and offset were determined from paired optode-bottle samples during ship visits to Ocean Station Papa (supporting information Figures S4–S9) or, for instrument 2 in June 2009, from paired optode-optode samples between deployments after adjustment of Instrument 1 to bottle samples (supporting information Figures S10 and S11). For instrument 1, an exponentially decreasing drift in sensitivity was assumed (equation (A1)) to constrain the gain and offset at the final comparison point (February 2010).

(University of Victoria) or S. Emerson (University of Washington) research groups (supporting information Data Set S1). Oxygen concentrations from bottle samples and optode sensors, the latter corrected for salinity and hydrostatic pressure effects (section 2), were converted to partial pressure pO_2 (Bittig, Körtzinger, Johnson, et al., 2018) before comparison along isopycnals or as averages within the surface layer. In most cases (see below), since Seaglider profiles were not performed at precisely the same location and time as bottle casts, an estimate of Seaglider pO_2 at the location and time of each bottle sample was obtained using a form of local regression estimation. For a given optode instrument, all samples within 15 days of the bottle sample along its same isopycnal or averaged within the surface layer were used to estimate a multivariable regression fit of the same form used to determine horizontal gradients (i.e., optode pO_2 as a function of x, y, t, and t^2; PEC1). This fit was evaluated at the location and time of the bottle sample to estimate the optode reading for comparison.

Abrupt temperature and oxygen changes were observed along isopycnals in the permanent pycnocline during Seaglider surveys (PEC1). For this reason, any bottle sample deeper than the surface layer whose temperature was outside the range observed by the comparison Seaglider along the same isopycnal within ±15 days was not used. For the February 2010 comparison casts (Table A1), which occurred while Seaglider

Table A1
Ship Bottle Casts With Independent Winkler Oxygen Measurements Used for Comparison to Optode Oxygen Samples in This Study

Vessel/cruise	Cast	Latitude	Longitude	Date	# Bottles (# used) top 1,000 m
CCGS *John P. Tully*	62	144°59.95′W	50°00.02′N	8 June 2008 22:26 UTC	5 (5)
2008-26	63	144°59.96′W	49°59.97′N	8 June 2008 23:46 UTC	1 (1)
—	75	144°49.95′W	50°08.28′N	10 June 2008 15:01 UTC	6 (4)
—	80	144°49.47′W	50°07.73′N	11 June 2008 19:27 UTC	5 (5)
R/V *Thomas G. Thompson*	301	144°50.02′W	50°05.49′N	30 August 2008 12:09 UTC	19 (16 Inst. 1, 10 Inst. 2)
TN224	302	144°48.35′W	50°05.54′N	30 August 2008 19:41 UTC	5 (4 Inst. 1, 2 Inst. 2)
Tully	65	144°50.12′W	50°07.96′N	14 June 2009 05:04 UTC	5 (5)
2009-09	74	145°0.03′W	50°00.01′N	14 June 2009 17:38 UTC	5 (5)
—	75	145°00.04′W	49°59.93′N	14 June 2009 20:15 UTC	6 (6)
—	76	144°59.98′W	49°59.96′N	14 June 2009 22:17 UTC	1 (1)
—	79	145°00.01′W	49°59.99′N	15 June 2009 02:31 UTC	5 (5)
—	80	145°00.06′W	49°59.97′N	15 June 2009 05:02 UTC	5 (5)
Tully	47	144°59.88′W	50°00.01′N	27 August 2009 19:57 UTC	4 (3)
2009-10	48	144°59.90′W	50°00.00′N	27August 2009 22:16 UTC	5 (5)
—	49	144°59.99′W	49°59.99′N	28 August 2009 00:34 UTC	5 (2)
—	51	145°00.02′W	50°00.06′N	28 August 2009 03:28 UTC	3 (2)
—	52	144°48.63′W	50°09.34′N	28 August 2009 07:29 UTC	5 (5)
Tully	37	138°39.94′W	49°33.98′N	8 February 2010 19:03 UTC	6 (6)
2010-01	41	138°39.97′W	49°34.07′N	9 February 2010 03:07 UTC	4 (4)

Note. All comparisons occurred near Ocean Station Papa with the exception of CCGS *Tully* cruise 2010-01 events 37/41, which were performed at station P20 on Line P. Deeper than the mixed layer, bottle samples were not used to compare to a given optode instrument if the bottle temperature was outside the range sampled by the instrument on the same isopycnal within ±15 days (Appendix A). Instrument 2 was not sampled deeper than 300 m during August 2008, reducing the number of bottles available for comparison.

144 was transiting along Line P, optode samples and positions were smoothed with a 1.5-day half-width triangular running mean filter and the values with the smallest spatial separation (2–3 km) from the ship casts were used for comparison, based on inspection of temperature along isopycnals. The resulting time separation was 2.4–2.8 days.

Following the factory calibration, optodes exhibit a consistent decrease in sensor gain with time since calibration, in addition to a small offset at zero oxygen concentration (Bittig, Körtzinger, Neill, et al., 2018). For each set of paired optode-bottle samples, referred to as a *comparison point*, a linear model was fit to optode versus bottle pO_2 to yield an estimate of sensor gain a and zero offset b. Supporting information Figures S4–S9 show plots of the paired samples and regression line at each comparison point, along with estimates of the 95% confidence interval of the regression line (Emery & Thomson, 2004, section 3.12.2) at a typical surface pO_2 of 210 mbar.

During deployment 2, Seaglider 120 ceased sampling 10 days prior to the June 2009 visit by the *Tully*. Due to this time gap, optode samples from the final 15 days of deployment 2 (instrument 2) were compared to samples from the initial 15 days of deployment 3 (instrument 1), with the latter having been adjusted to match the June 2009 bottle samples, along isopycnals in intervals of 0.2 kg/m^3 (supporting information Figure S10). The resulting comparison has similar precision to the ship-optode comparison points (supporting information Figure S11).

Both sensors exhibit an overall decline in gain versus time (Figure A1a) and a modest increase in zero offset (Figure A1b), with the exception of instrument 1 at its final comparison point (February 2010), whose coefficients are more uncertain due to bottle samples being available only in the upper 200 m. Based on the consistent decline with time of other optodes (Bittig, Körtzinger, Neill, et al., 2018, their Figure 7), it is unlikely that the instrument 1 gain increased between August 2009 and February 2010. The estimated instrument 1 gain values were fit with a function (Bittig, Körtzinger, Neill, et al., 2018):

$$\hat{a}(t) = 1 + A\left(e^{-\frac{(t-t0)}{\tau}} - 1\right), \tag{A1}$$

with weighting inversely proportional to the size of the confidence bounds on each gain estimate, and t_0 = 8 June 2008. The results (A = 0.11, τ = 1.21 year) were used to estimate a gain value of 0.9146 for February 2010 (Figure A1a), which was used with the February 2010 optode-bottle paired samples to determine an estimated zero offset of −0.5096 mbar (Figure A1b and supporting information Figure S9).

Optode samples $pO_{2(\mathrm{opt})}$ were adjusted according to

$$pO_{2(\mathrm{opt},a)} = \frac{1}{a(t)} pO_{2(\mathrm{opt})} - \frac{b(t)}{a(t)}, \tag{A2}$$

where $a(t)$ and $b(t)$ are determined for each instrument as described above and linearly interpolated in time between comparison points. Given the long time scales of the decline in optode sensitivity, a linear interpolation of gain over intervals of several months gives similar results to the decay (A1) (Figure A1a). Adjusted optode partial pressures $pO_{2(\mathrm{opt},a)}$ were converted back to oxygen concentrations before estimating the quantities described in section 2.

Acknowledgments
The National Science Foundation (NSF) supported Seaglider observations at OSP and analysis of these data under grants OCE-0628663 and OCE-1129090. The NOAA surface mooring was funded in 2007-08 by NSF grant OCE-0628663 and thereafter by the Ocean Observing and Monitoring Division, Climate Programs Office, NOAA DOC. This research was completed while NAP was a postdoctoral researcher at the University of Washington Joint Institute for the Study of the Atmosphere and Ocean and NOAA Alaska Fisheries Science Center Marine Mammal Laboratory. C. Stump, S. Bushinsky, K. Giesbrecht, A. Lara, and R. Hamme generously provided Line P oxygen measurements for Seaglider calibration. Many helpful discussions with S. Bushinsky, A. Fassbender, H. Palevsky, T. Hennon, B. Yang, C. Schallenberg, and A. Timmerman informed this work. The authors are grateful to two anonymous reviewers whose comments helped to strengthen this manuscript. Thanks to M. Robert and the DFO-Canada Line P Program for making these observations possible. This is Pacific Marine Environmental Laboratory contribution 4642. Seaglider data are available at the original sampling resolution from the National Oceanographic Data Center at https://www.nodc.noaa.gov/. Bin-averaged Seaglider data are available from the University of Washington Researchworks Archive at http://hdl.handle.net/1773/41656. MATLAB code for loading and manipulating the bin-averaged data and creating example plots is available at https://github.com/noelpelland/SG-at-OSP/. Bottle oxygen data are available in the supporting information (Data Set S1). Data from WOA13 are available at http://www.nodc.noaa.gov/OC5/woa13/. Advanced scatterometer wind products were obtained from the Asia-Pacific Data Research Center at http://apdrc.soest.hawaii.edu/datadoc/ascat.php. The NCEP/NCAR Reanalysis 1 data were provided by the NOAA/OAR/ESRL PSD, Boulder, Colorado, USA, from their Web site at http://www.esrl.noaa.gov/psd/. The AVISO *all-satellite* Absolute Dynamic Topography sea surface height estimates are available from the European Copernicus Marine Environment Monitoring Service at http://marine.copernicus.eu/.

References

Aanderaa Data Instruments (2004). TD218 operating manual: Oxygen optode 3830, 3930, 3975, 3835, 4130 and 4175.

Alkire, M., D'Asaro, E., Lee, C., Perry, M., Gray, A., Cetinić, et al. (2012). Estimates of net community production and export using high-resolution, Lagrangian measurements of O_2, NO_3^-, and POC through the evolution of a spring diatom bloom in the North Atlantic. *Deep-Sea Research I*, *64*, 157–174.

Bentamy, A., & Croize-Fillon, D. (2012). Gridded surface wind fields from Metop/ASCAT measurements. *International Journal of Remote Sensing*, *33*(6), 1729–1754.

Bittig, H. C., Fiedler, B., Scholz, R., Krahmann, G., & Körtzinger, A. (2014). Time response of oxygen optodes on profiling platforms and its dependence on flow speed and temperature. *Limnology and Oceanography: Methods*, *12*, 617–636. https://doi.org/10.4319/lom.2014.12.617

Bittig, H. C., & Körtzinger, A. (2017). Technical note: Update on response times, in-air measurements, and in situ drift for oxygen optodes on profiling platforms. *Ocean Science*, *13*, 1–11.

Bittig, H. C., Körtzinger, A., Johnson, K. S., Claustre, H., Emerson, S. R., Fennel, K., et al. (2018). *SCOR WG 142: Quality control procedures for oxygen and other biogeochemical sensors on floats and gliders. Recommendations on the conversion between oxygen quantities for Bio-Argo floats and other autonomous sensor platforms* (v1.1). France: Ifremer Plouzane. https://doi.org/10.13155/45915

Bittig, H. C., Körtzinger, A., Neill, C., van Ooijen, E., Plant, J. N., Hahn, J., et al. (2018). Oxygen optode sensors: Principle, characterization, calibration, and application in the ocean. *Frontiers in Marine Science*, *4*, 429. https://doi.org/10.3389/fmars.2017.00429

Boyer, T., Antonov, J., Baranova, O., Coleman, C., Garcia, H., Grodsky, A., et al. (2013). World Ocean Database 2013. In S. Levitus & A. Mishonov (Eds.), *NOAA Atlas NESDIS 72*. Silver Spring, MD: NOAA National Oceanographic Data Center. https://doi.org/10.7289/V5NZ85MT

Brix, H., Gruber, N., Karl, D. M., & Bates, N. R. (2006). On the relationships between primary, net community, and export production in subtropical gyres. *Deep-Sea Research*, *II*(53), 698–717.

Burchard, H. (2002). *Applied Turbulence Modelling in Marine Waters*. Berlin: Springer-Verlag.

Bushinsky, S. M., & Emerson, S. R. (2015). Marine biological production from in situ oxygen measurements on a profiling float in the subarctic Pacific Ocean. *Global Biogeochemical Cycles*, *29*, 2050–2060. https://doi.org/10.1002/2015GB005251

Cronin, M., Pelland, N., Crawford, W., & Emerson, S. (2015). Estimating diffusivity from the mixed layer heat and salt balances in the North Pacific. *Journal of Geophysical Research: Oceans*, *120*, 7346–7362. https://doi.org/10.1002/2015JC011010

Cummins, P., & Masson, D. (2012). Wind-driven variability of dissolved oxygen below the mixed layer at Station P. *Journal of Geophysical Research*, *117*, C08015. https://doi.org/10.1029/2011JC007847

Emerson, S. (1987). Seasonal oxygen cycles and biological new production in surface waters of the subarctic Pacific Ocean. *Journal of Geophysical Research*, *92*(C6), 6535–6544.

Emerson, S. (2014). Annual net community production and the biological carbon flux in the ocean. *Global Biogeochemical Cycles*, *28*, 1–12. https://doi.org/10.1002/2013GB004680

Emerson, S., & Bushinsky, S. (2016). The role of bubbles during air-sea gas exchange. *Journal of Geophysical Research: Oceans*, *121*, 4360–4376. https://doi.org/10.1002/2016JC011744

Emerson, S., & Hedges, J. (2008). *Chemical Oceanography and the Marine Carbon Cycle*. New York: Cambridge University Press.

Emerson, S., Quay, P., Karl, D., Winn, C., Tupas, L., & Landry, M. (1997). Experimental determination of the organic carbon flux from open-ocean surface waters. *Nature*, *389*, 951–954.

Emerson, S., Quay, P., Stump, C., Wilbur, D., & Knox, M. (1991). O_2, Ar, N_2, and ^{222}Rn in surface waters of the subarctic ocean: Net biological O_2 production. *Global Biogeochemical Cycles*, *5*(1), 49–69.

Emerson, S., & Stump, C. (2010). Net biological oxygen production in the ocean—II: Remote in situ measurements of O_2 and N_2 in subarctic Pacific surface waters. *Deep-Sea Research I*, *57*, 1255–1265.

Emerson, S., Stump, C., & Nicholson, D. (2008). Net biological oxygen production in the ocean: Remote in situ measurements of O_2 and N_2 in surface waters. *Global Biogeochemical Cycles*, *22*, GB3023. https://doi.org/10.1029/2007GB003095

Emery, W., & Thomson, R. E. (2004). *Data Analysis Methods in Physical Oceanography* (2nd ed.). Amsterdam: Elsevier.

Falkowski, P., Scholes, R., Boyle, E., Canadell, J., Canfield, D., Elser, J., et al. (2000). The global carbon cycle: A test of our knowledge of Earth as a system. *Science*, *290*, 291–296.

Fassbender, A., Sabine, C., & Cronin, M. (2016). Net community production and calcification from seven years of NOAA station Papa mooring measurements. *Global Biogeochemical Cycles*, *30*, 250–267. https://doi.org/10.1002/2015GB005205

Feely, R., Sabine, C., Schlitzer, R., Bullister, J., Mecking, S., & Greeley, D. (2004). Oxygen utilization and organic carbon remineralization in the upper water column of the Pacific Ocean. *Journal of Oceanography*, *60*, 45–52.

Freeland, H. J. (2013). Evidence of change in the winter mixed layer in the Northeast Pacific Ocean: A problem revisited. *Atmosphere-Ocean*, *51*(1), 126–133.

Garcia, H., & Gordon, L. (1992). Oxygen solubility in seawater: Better fitting equations. *Limnology and Oceanography*, *37*(6), 1307–1312.
Giesbrecht, K., Hamme, R., & Emerson, S. (2012). Biological productivity along Line P in the subarctic Northeast Pacific: In situ versus incubation-based methods. *Global Biogeochemical Cycles*, *26*, GB3028. https://doi.org/10.1029/2012GB004349
Gill, A. (1982). *Atmosphere-Ocean Dynamics*. San Diego, CA: Academic Press.
Hamme, R., & Emerson, S. (2006). Constraining bubble dynamics and mixing with dissolved gases: Implications for productivity measurements by oxygen mass balance. *Journal of Marine Research*, *64*, 73–95.
Hamme, R., Webley, P., Crawford, W., Whitney, F., DeGrandpre, M., Emerson, S., et al. (2010). Volcanic ash fuels anomalous plankton bloom in subarctic northeast Pacific. *Geophysical Research Letters*, *37*, L19604. https://doi.org/10.1029/2010GL044629
Hedges, J., Baldock, J., Gelinas, Y., Lee, C., Peterson, M., & Wakeham, S. (2002). The biochemical and elemental compositions of marine plankton: A NMR perspective. *Marine Chemistry*, *45*, 47–63.
Hennon, T. D., Riser, S. C., & Mecking, S. (2016). Profiling float-based observations of net respiration beneath the mixed layer. *Global Biogeochemical Cycles*, *30*, 920–932. https://doi.org/10.1002/2016GB005380
Howard, E., Emerson, S., Bushinsky, S., & Stump, C. (2010). The role of net community production in air-sea carbon fluxes at the North Pacific subarctic-subtropical boundary region. *Limnology and Oceanography*, *55*(6), 2585–2596.
Izett, R. W., Manning, C. C., Hamme, R. C., & Tortell, P. D. (2018). Refined estimates of net community production in the subarctic Northeast Pacific derived from $\Delta O_2/Ar$ measurements with N_2O-based corrections for vertical mixing. *Global Biogeochemical Cycles*, *32*, 326–350. https://doi.org/10.1002/2017GB005792
Juranek, L., Quay, P., Feely, R., Lockwood, D., Karl, D., & Church, M. (2012). Biological production in the NE Pacific and its influence on air-sea CO_2 flux: Evidence from dissolved oxygen isotopes and O_2/Ar. *Journal of Geophysical Research*, *117*, C05022. https://doi.org/10.1029/2011JC007450
Kalnay, E., Kanamitsu, M., Kistler, R., Collins, W., Deaven, D., Gandin, L., et al. (1996). The NCEP/NCAR 40-year reanalysis project. *Bulletin of the American Meteorological Society*, *77*(3), 437–471.
Körtzinger, A., Send, U., Lampitt, R. S., Hartman, S., Wallace, D. W. R., Karstensen, J., et al. (2008). The seasonal pCO_2 cycle at 49°N/16.5°W in the northeastern Atlantic Ocean and what it tells us about biological productivity. *Journal of Geophysical Research*, *113*, C04020. https://doi.org/10.1029/2007JC004347
Kundu, P. K., & Cohen, I. M. (2008). *Fluid Mechanics* (4th ed.) San Diego, CA: Academic Press.
Large, W., McWilliams, J., & Doney, S. (1994). Oceanic vertical mixing: A review and a model with a nonlocal boundary layer parameterization. *Reviews of Geophysics*, *32*, 363–403.
Liang, J.-H., Deutsch, C., McWilliams, J., Baschek, B., Sullivan, P., & Chiba, D. (2013). Parameterizing bubble-mediated air-sea gas exchange and its effect on ocean ventilation. *Global Biogeochemical Cycles*, *27*, 894–905. https://doi.org/10.1002/gbc.20080
Lockwood, D., Quay, P., Kavanaugh, M., Juranek, L., & Feely, R. (2012). High-resolution estimates of net community production and air-sea CO_2 flux in the Northeast Pacific. *Global Biogeochemical Cycles*, *26*, GB4010. https://doi.org/10.1029/2012GB004380
Martin, P. (1985). Simulation of the mixed layer at OWS November and Papa with several models. *Journal of Geophysical Research*, *90*(C1), 903–916.
Martz, T., Johnson, K., & Riser, S. (2008). Ocean metabolism observed with oxygen sensors on profiling floats in the South Pacific. *Limnology and Oceanography*, *53*(5), 2094–2111.
Nicholson, D. P. (2009). Nitrogen, oxygen and the noble gases as tracers of upper-ocean productivity and air-sea gas fluxes (PhD thesis), University of Washington.
Nicholson, D., Emerson, S., & Eriksen, C. (2008). Net community production in the deep euphotic zone of the subtropical North Pacific gyre from glider surveys. *Limnology and Oceanography*, *53*(5), 2226–2236.
Nicholson, D. P., & Feen, M. L. (2017). Air calibration of an oxygen optode on an underwater glider. *Limnology and Oceanography: Methods*, *15*, 495–502.
Omand, M. M., D'Asaro, E. A., Lee, C. M., Perry, M. J., Briggs, N., Cetinić, I., & Mahadevan, A. (2015). Eddy-driven subduction exports particulate organic carbon from the spring bloom. *Science*, *348*(6231), 222–225.
Oschlies, A., & Kähler, P. (2004). Biotic contribution to air-sea fluxes of CO_2 and O_2 and its relation to new production, export production, and net community production. *Global Biogeochemical Cycles*, *18*, GB1015. https://doi.org/10.1029/2003GB002094
Palevsky, H. I., Quay, P. D., Lockwood, D. E., & Nicholson, D. P. (2016). The annual cycle of gross primary production, net community production, and export efficiency across the North Pacific Ocean. *Global Biogeochemical Cycles*, *30*, 361–380. https://doi.org/10.1002/2015GB005318
Pelland, N. (2015). Eddy circulation, heat and salt balances, and ocean metabolism: Observations from a Seaglider-Mooring array at Ocean Station Papa (Ph.D. thesis), University of Washington, Seattle, WA. https://doi.org/hdl.handle.net/1773/35285
Pelland, N. A., Eriksen, C. C., & Cronin, M. F. (2016). Seaglider surveys at Ocean Station Papa: Circulation and water mass properties in a meander of the North Pacific current. *Journal of Geophysical Research: Oceans*, *121*, 6816–6846. https://doi.org/10.1002/2016JC011920
Pelland, N. A., Eriksen, C. C., & Cronin, M. F. (2017). Seaglider surveys at Ocean Station Papa: Diagnosis of upper-ocean heat and salt balances using least squares with inequality constraints. *Journal of Geophysical Research: Oceans*, *122*, 5140–5168. https://doi.org/10.1002/2017JC012821
Pelland, N., Sterling, J., Lea, M.-A., Bond, N., Ream, R., Lee, C., & Eriksen, C. (2014). Fortuitous encounters between seagliders and adult female northern fur seals (Callorhinus ursinus) off the Washington (USA) coast: Upper ocean variability and links to top predator behavior. *PLoS ONE*, *9*(8), e101268. https://doi.org/10.1371/journal.pone.0101268
Perry, M., Sackmann, B., Eriksen, C., & Lee, C. (2008). Seaglider observations of blooms and subsurface chlorophyll maxima off the Washington coast. *Limnology and Oceanography*, *53*(5), 2169–2179.
Plant, J. N., Johnson, K. S., Sakamoto, C. M., Jannasch, H. W., Coletti, L. J., Riser, S. C., & Swift, D. D. (2016). Net community production at Ocean Station Papa observed with nitrate and oxygen sensors on profiling floats. *Global Biogeochemical Cycles*, *30*, 859–879. https://doi.org/10.1002/2015GB005349
Quay, P., Stutsman, J., & Steinhoff, T. (2012). Primary production and carbon export rates across the subpolar N. Atlantic Ocean basin based on triple oxygen isotope and dissolved O_2 and Ar gas measurements. *Global Biogeochemical Cycles*, *26*, GB2003. https://doi.org/10.1029/2010GB004003
Riser, S., & Johnson, K. (2008). Net production of oxygen in the subtropical ocean. *Nature*, *451*(17), 323–326.
Sackmann, B. S. (2007). Remote assessment of 4-D phytoplankton distributions off the Washington coast (Ph.D. thesis), University of Maine.
Sackmann, B. S., Perry, M. J., & Eriksen, C. C. (2008). Seaglider observations of variability in daytime fluorescence quenching of chlorophyll-a in Northeastern Pacific coastal waters. *Biogeosciences Discussions*, *5*, 2839–2865.
Steiner, N., Vagle, S., Kenman, K., & McNeil, C. (2007). Oxygen and nitrogen cycling in the Northeast Pacific—Simulations and observations at station Papa in 2003/2004. *Journal of Marine Research*, *65*, 441–469.

Tabata, S. (1965). Variability of oceanic conditions at station "P" in the Northeast Pacific Ocean. *Transactions of the Royal Society of Canada*, *4*, 367–478.

Thomas, F., Garcon, V., & Minster, J.-F. (1990). Modelling the seasonal cycle of dissolved oxygen in the upper ocean at ocean weather station P. *Deep-Sea Research*, *37*(3), 463–491.

Thomsen, S., Kanzow, T., Colas, F., Echevin, V., Krahmann, G., & Engel, A. (2016). Do submesoscale frontal processes ventilate the oxygen minimum zone off Peru? *Geophysical Research Letters*, *43*, 8133–8142. https://doi.org/10.1002/2016GL070548

Uchida, H., Kawano, T., Ikuo, K., & Masao, F. (2008). In situ calibration of optode-based oxygen sensors. *Journal of Atmospheric and Oceanic Technology*, *25*, 2271–2281.

Whitney, F., & Freeland, H. (1999). Variability in upper-ocean water properties in the NE Pacific Ocean. *Deep-Sea Research II*, *46*, 2351–2370.

Woolf, D., & Thorpe, S. (1991). Bubbles and the air-sea exchange of gases in near-saturation conditions. *Journal of Marine Research*, *49*, 435–466.

Yang, B., Emerson, S. R., & Bushinsky, S. M. (2017). Annual net community production in the subtropical Pacific Ocean from in situ oxygen measurements on profiling floats. *Global Biogeochemical Cycles*, *31*, 728–744. https://doi.org/10.1002/2016GB005545